Infrared Spectroscopy with Multivariate Analysis Potentially Facilitates the Segregation of Different Types of Prostate Cell

Matthew J. German,*† Azzedine Hammiche,* Narasimhan Ragavan,†‡ Mark J. Tobin,§ Leanne J. Cooper,† Shyam S. Matanhelia,‡ Andrew C. Hindley,‡ Caroline M. Nicholson,‡ Nigel J. Fullwood,† Hubert M. Pollock,* and Francis L. Martin†

*Department of Physics, Lancaster University, Lancaster LA1 4YB, United Kingdom; †Biomedical Sciences Unit, Lancaster University, Lancaster LA1 4YQ, United Kingdom; ‡Lancashire Teaching Hospitals Trust, Preston, United Kingdom; and §Synchrotron Radiation Department, CCLRC Daresbury Laboratory, Warrington, United Kingdom

ABSTRACT The prostate gland is conventionally divided into zones or regions. This morphology is of clinical significance as prostate cancer (CaP) occurs mainly in the peripheral zone (PZ). We obtained tissue sets consisting of paraffin-embedded blocks of cancer-free transition zone (TZ) and PZ and adjacent CaP from patients ($n = 6$) who had undergone radical retropubic prostatectomy; a seventh tissue set of snap-frozen PZ and TZ was obtained from a CaP-free gland removed after radical cystoprostatectomy. Paraffin-embedded tissue slices were sectioned (10-μm thick) and mounted on suitable windows to facilitate infrared (IR) spectra acquisition before being dewaxed and air dried; cryosections were dessicated on BaF_2 windows. Spectra were collected employing synchrotron Fourier-transform infrared (FTIR) microspectroscopy in transmission mode or attenuated total reflection-FTIR (ATR) spectroscopy. Epithelial cell and stromal IR spectra were subjected to principal component analysis to determine whether wavenumber-absorbance relationships expressed as single points in "hyperspace" might on the basis of multivariate distance reveal biophysical differences between cells in situ in different tissue regions. After spectroscopic analysis, plotted clusters and their loadings curves highlighted marked variation in the spectral region containing DNA/RNA bands ($\approx$1490–1000 cm^{-1}). By interrogating the intrinsic dimensionality of IR spectra in this small cohort sample, we found that TZ epithelial cells appeared to align more closely with those of CaP while exhibiting marked structural differences compared to PZ epithelium. IR spectra of PZ stroma also suggested that these cells are structurally more different to CaP than those located in the TZ. Because the PZ exhibits a higher occurrence of CaP, other factors (e.g., hormone exposure) may modulate the growth kinetics of initiated epithelial cells in this region. The results of this pilot study surprisingly indicate that TZ epithelial cells are more likely to exhibit what may be a susceptibility-to-adenocarcinoma spectral signature. Thus, IR spectroscopy on its own may not be sufficient to identify premalignant prostate epithelial cells most likely to progress to CaP.

INTRODUCTION

The human prostate gland is a composite organ consisting of a nonglandular (fibromuscular) component variously interspersed with glandular elements (1). This architectural complexity is made further intricate by the presence of blood vessels, nerves, neuroendocrine cells, and aggregated glycoprotein deposits. With the urethra as the key anatomical reference point, the prostate is also conventionally divided into three tightly fused zones, or regions, known as the peripheral zone (PZ), the transition zone (TZ), and the central zone (CZ) (2). The clinical significance of this complex morphology is that the multifocal entity of prostate adenocarcinoma (CaP) arises mostly in the PZ, whereas benign prostatic hypertrophy (BPH), a nonmalignant overgrowth, appears to arise exclusively from the TZ (1). Identification of a "susceptibility-to-adenocarcinoma spectral signature" based on biochemical cell structural characteristics could facilitate the identification of premalignant cells (3).

CaP is the most common malignancy in men and the second-leading cause of male cancer-related death in developed countries (4,5). Its progression is a multistage process from latent carcinoma(s) of low histological grade to high-grade metastatic disease (6). In developed countries, the lifetime risk of developing CaP is ~1 in 6 (7). Incidence increases proportionally with age, and among 80-year-old men, ~80% have CaP foci (8). Risk factors may include race, androgen levels, genetic predisposition, and/or diet (9). Studies of migrant populations from low-risk to high-risk regions point to an association with Western-related lifestyles (10). CaP accounts for 15.3% of all cancers occurring in men in developed countries and 4.3% in developing countries (6,11). However, to date the only factor known to be associated with CaP is increasing age (12).

Fourier-transform infrared (FTIR) microspectroscopy may discriminate between disease-free cells and those of pathological regions, e.g., cancerous (13). Cellular biomolecules absorb the midinfrared (λ = 2–20 μm) via vibrational transitions that are derived from individual chemical bonds;

Submitted November 7, 2005, and accepted for publication February 7, 2006.

Address reprint requests to Dr. Francis L. Martin, Biomedical Sciences Unit, Lancaster University, Lancaster LA1 4YQ, UK. Tel.: 44-1524-594505; Fax: 44-1524-593192; E-mail: f.martin@lancaster.ac.uk.

Matthew J. German's present address is School of Dental Sciences, Framlington Place, University of Newcastle, Newcastle NE2 4BW, UK.

Mark J. Tobin's present address is Australian Synchrotron Project, Blackburn Rd., Victoria, Australia.

0006-3495/06/05/3783/13 $2.00

doi: 10.1529/biophysj.105.077255

this may yield richly structured ''fingerprint'' spectra relating to structure and conformation (14–17). Conventional FTIR spectrometers are equipped with a globar source that is a relatively dim thermal infrared (IR) source compared to a synchrotron IR source (18). In IR microscopy, the beam width must be limited and if an aperture of, say, 5 μm $\times$ 5 μm is employed, in an attempt to achieve high spatial resolution, the signal/noise (S/N) ratio is seriously degraded. Synchrotron IR sources generate a highly collimated beam of photons that is of higher brilliance and may be delivered through a very small sampling aperture to improve the spatial resolution up to the point at which it becomes diffraction limited. This allows for the acquisition of spectra at a spatial resolution of 5 μm and S/N ratio $\sim$1000 times greater than conventional FTIR microspectroscopy (18,19). Attenuated total reflection-FTIR (ATR) spectroscopy is another method that is particularly suited for the IR interrogation of membrane-associated peptides and proteins (16).

Large numbers of variables, as found in some spectroscopic studies, make it difficult to identify the significant underlying variance (14,19). The intrinsic dimensionality of such data may be interrogated using principal component analysis (PCA). In PCA, each spectrum becomes a single point, or score, in n-dimensional space and using selected principal components (PCs) as coordinates, the data may be analyzed for clustering when viewed in a particular direction. The PCs are eigenvectors of the correlation coefficient matrix of squared deviations. They comprise a new set of variables, retaining almost all the variation present in all of the original spectral variables, with the first PC presenting the most variance, the second PC (orthogonal to PC1) presenting the maximum amount of the remaining variance, etc. (20).

Once the clusters have been identified, one needs to define those regions of the spectra that exhibit biomolecular and/or conformational changes. Accordingly, PCA also estimates the contribution of each wavenumber (loadings or weight) to each PC. PCA then allows a loadings curve, or pseudospectrum, to be plotted for each PC, in effect giving the variance at each wavenumber in the spectrum. A possible weakness of this approach is that unless one of the PCs happens to pass through the cluster in question, the vital wavenumbers responsible for the observed clustering might be missed. The identification of a given cluster involves more than one PC and we show that a single ''cluster vector'' may be plotted, passing through the median of the cluster of interest. A weighted averaging algorithm then gives a single loadings curve.

In this study, we employed ATR spectroscopy and synchrotron radiation-based FTIR microspectroscopy to examine the CaP-free spectral signature of PZ and TZ glandular epithelial cells in comparison with those in histologically designated CaP regions. The stromal matrices in which such cell types are held were also interrogated. The rationale of this approach was to determine whether spectrally designated structural characteristics could be identified that might point to a region-specific susceptibility to adenocarcinoma within the prostate. If a susceptibility-to-adenocarcinoma spectral signature could be identified using IR spectroscopy, such an approach could facilitate the monitoring and identification of premalignant cells before progression to invasive CaP.

MATERIALS AND METHODS

Study participants

Informed consent to obtain prostate tissue sets for research was obtained (LREC no. 2003.6.v; Preston, Chorley, and South Ribble Ethical Committee). Patients ($n = 6$; Table 1) undergoing radical retropubic prostatectomy (RRP) for CaP on the basis of low PSA ($<$20 μg/l serum) and low-disease volume (less than two core CaP-positive biopsies per eight taken) were selected (3). In addition, after a radical cystoprostatectomy for removal of muscle-invasive bladder carcinoma, a seventh CaP-free tissue set was obtained (Table 1). The donor patient cohort was coded PEC1–PEC7 with PEC1–PEC6 being samples obtained from RRP patients; PEC7 was the seventh tissue. From each donor patient, a tissue set consisting of separate slices of CaP-free PZ, CaP-free TZ, and CaP was obtained.

Prostate tissue sets

To this end, a CaP-free prostate tissue mass separate to the area of CaP, that would be present in the gland, was isolated postsurgery. Tissue slices representing the PZ or TZ tissue were dissected out from these tissue masses. Independently of this procedure, a slice containing CaP and isolated from a different part of the prostate gland (i.e., separate to the aforementioned tissue mass) was also retrieved. Subsequently, a microtomed 10-μm-thick section of each tissue slice was prepared for analysis by IR spectroscopy.

After each individual RRP, a CaP-free prostate tissue mass was selected from the lobe from which preoperative biopsy cores were negative. This prostate tissue mass was sliced from the upper part of the gland just above the area of the verumontanum. To obtain PZ tissue, a slice $\sim$2 cm in length and 0.3 cm in width was isolated from the most peripheral and posterolateral aspect of the gland. A further tissue slice, $\sim$1.5 cm in length and 0.3 cm in width, was then isolated from the area identified immediately lateral to the urethra (periurethral); this was designated TZ. These tissue slices were immediately formalin fixed, after which they were paraffin embedded. Also after RRP, a representative paraffin-embedded slice containing CaP was obtained through the hospital pathology archive in which all such tissues are stored indefinitely. Microtomed sections (4-μm thick) of all these paraffin-embedded tissue slices were stained with hematoxylin and eosin (H&E) to be checked retrospectively by a pathologist to confirm the absence of CaP or

TABLE 1 Details of study participants and tissue samples examined

Patient no.	Age (year)	PSA (μg/l)	DRE	Smoking status	Alcohol	Diet	Gleason grade
PEC1	62	9.0	Benign	Yes	Yes	NV	4+3
PEC2	59	4.4	Benign	Yes	Yes	NV	3+4
PEC3	60	5.4	Benign	Yes	Yes	NV	3+3
PEC4	68	4.4	Benign	No	Yes	NV	3+4
PEC5	65	8.0	T_2 right lobe	Yes	No	NV	4+3
PEC6	58	4.6	Benign	No	Yes	NV	3+3
PEC7*	68	0.5	Benign	Yes	No	NV	NA

*Cystoprostatectomy sample.

Patients who donated prostate tissue sets for the purposes of this study were chronologically numbered PEC1–PEC7. Tumors were distinguished histologically according to Gleason grade. Abbreviations used: DRE, digital rectal examination; NV, nonvegetarian; PSA, prostate-specific antigen; NA, not applicable.

to demarcate the diseased tissue area. After radical cystoprostatectomy, small tissue slices of designated PZ or TZ were isolated as before prior to immediate snap freezing in liquid N_2 and storage at −85°C. An adjacent small tissue slice was formalin fixed for subsequent histological examination, i.e., paraffin embedding and subsequent staining with H&E.

Tissue preparation for spectroscopy

From RRP patients (PEC1–PEC6), tissue sets consisting of paraffin-embedded PZ, TZ, and CaP tissue slices were obtained. Cut from these tissue slices, microtomed 10-μm-thick sections of tissue were floated onto either 1 cm × 1 cm Low-E reflective glass microscope slides (for ATR spectroscopy) or 0.5-mm-thick BaF_2 windows (Photox Optical Systems, Sheffield, UK) (for transmission-mode synchrotron FTIR microspectroscopy). Sections themselves embedded in wax would contain no water, but the surface water between the section and the glass slides or BaF_2 windows was dried off overnight at 37°C. The sections were then dewaxed by immersion in xylene (5 min) and then washed in absolute alcohol (74OP) (5 min, i.e., to remove the xylene). In clearly labeled petri dishes, the sections were then placed under vacuum overnight to facilitate removal of atmospheric water, after which they were stored in a dessicator until analysis. Cryosections (10-μm thick) of snap-frozen samples (PEC7) were placed on 0.5-mm-thick BaF_2 windows, placed under vacuum overnight, and then in a dessicator until analysis with synchrotron FTIR microspectroscopy.

ATR spectroscopy

Spectra were acquired using a Bruker Vector 22 FTIR spectrometer with Helios ATR attachment that contained a diamond crystal (Bruker Optics, Billerica, MA). Using a closed circuit television camera attached to the ATR crystal, tissue architecture was examined to identify specific regions for analysis. Data were collected in ATR mode and spectra (8 cm^{-1} spectral resolution, coadded for 32 scans) were converted into absorbance using Bruker OPUS software. Spectra were acquired from glandular elements or surrounding stroma. Sodium dodecyl sulfate (Sigma Chemical, Poole, Dorset, UK) was used to clean the ATR crystal after every five spectral acquisitions, before transfer of analysis of glandular elements to stroma or before the first spectral analysis of a particular sample. Each time the crystal was cleaned a new background reading was also taken before recommencing spectral analysis. Spectra were baseline corrected using OPUS software and normalized to the amide II (≈1533 cm^{-1}) absorbance band.

Synchrotron FTIR microspectroscopy

Spectra were acquired at Daresbury (Warrington, UK) synchrotron source on beamline 11.1 using the Thermo Nicolet continuum microscope and Nexus FTIR spectrometer. Spectral collection was in transmission mode, and spectra were converted to absorbance using Thermo Omnic software (Waltham, MA). A 32× Reflachromat objective was used, and the aperture area was 10 μm × 10 μm. Spectra were collected at 4 cm^{-1} spectral resolution and coadded for 1024 scans.

In CaP-free tissues (PZ or TZ), five independent spectral measurements were taken on each of three randomly chosen glandular elements and adjacent stroma. In CaP regions, three independent spectral measurements were taken on each of five randomly chosen glandular elements and five spectral measurements were taken of adjacent stroma. During FTIR analyses a new background was taken every 2 h and/or before commencing analysis of another sample. Spectra were baseline corrected using OPUS software and normalized to the amide II (≈1533 cm^{-1}) absorbance band.

Biochemical spectral derivations

After baseline correction and normalization to amide II, the ratio of nucleic acids (RNA/DNA) was determined as the absorbance ratio of band intensities at 1121 cm^{-1} and 1020 cm^{-1} (13). This was derived using OPUS software as was the integrated absorbance of the carbohydrate region (900–1185 cm^{-1}) and nucleic acid phosphates (1185–1300 cm^{-1}) (13).

Statistical analysis

All spectra were processed as first derivative (15 points) after baseline correction and normalization, employing PCA conducted using the Pirouette software package (Infometrix, Woodinville, WA) (14). As mentioned above, to derive an accurate loadings curve (pseudospectrum) to define those regions of the spectra that exhibit biomolecular and/or conformational changes, we developed a semigraphical method that constructs a ''cluster vector'', passing through the median of the cluster (see Supplementary Material). A cluster vector does not represent a real PC as it is not orthogonal to the real PCs. However, its loadings curve may be calculated simply by taking a weighted average of the components of the loadings of three real PCs that were used to identify the cluster. This weighted averaging is done on the basis of simple vector algebra (see Supplementary Material): using the Pirouette loadings spreadsheet for each PC in turn, its eigenvalue is multiplied by the cosine of the angle through which it has been projected onto the plane of view in hyperspace in which the cluster vector is located. It is further multiplied by the cosine of the angle that it makes with the cluster vector. The weighting factor thus derived is then used to multiply this PC's loadings for all wavenumbers. The same is done for the remaining two PCs. Then for each wavenumber, these weighted loadings are added and the resultant data give a single loadings curve for the cluster in question.

Electron microscopy

After dissection, prostate tissue fragments (~50 mg; PZ PEC4) were placed in glutaraldehyde (4% in 0.1 M sodium cacodylate buffer). After fixation, tissues were washed in sodium cacodylate buffer, postfixed in osmium tetroxide, dehydrated in an alcohol series, and embedded in araldite resin. Ultrathin sections (70 nm) were cut on a Reichert Ultracut E ultramicrotome (Reichert-Jung, Wien, Austria) and stained with 2% uranyl acetate and lead citrate before being examined on a JEOL JEM-1010 transmission electron microscope (JEOL, Tokyo, Japan) (3).

RESULTS

Prostate tissue architecture

Electron microscopy showed secretory columnar cells sitting on flattened basal cells attached to a basement membrane in CaP-free prostate glands (Fig. 1 *A*). With increasing Gleason grade, increasing dedifferentiation compared to CaP-free tissue occurs (21). Only patients preoperatively diagnosed with low-grade carcinoma were recruited into this study. This approach allowed us the possibility to interrogate using IR spectroscopy, relatively normal tissue independently of and in comparison to CaP. Ultrastructural analysis of epithelial cells lining CaP glands (Fig. 1 *B*) clearly showed the presence of an increased number of vesicles (i.e., white circular entities in the cytoplasm of these cells). This could be associated with an elevated secretion of extracellular material. The double-cell epithelial architecture (i.e., secretory columnar cells sitting on flattened basal cells) characteristic of CaP-free prostate glands was also apparent after H&E staining (Fig. 1 *C*). PZ tissue architecture was characterized by the presence of many glandular elements with relatively

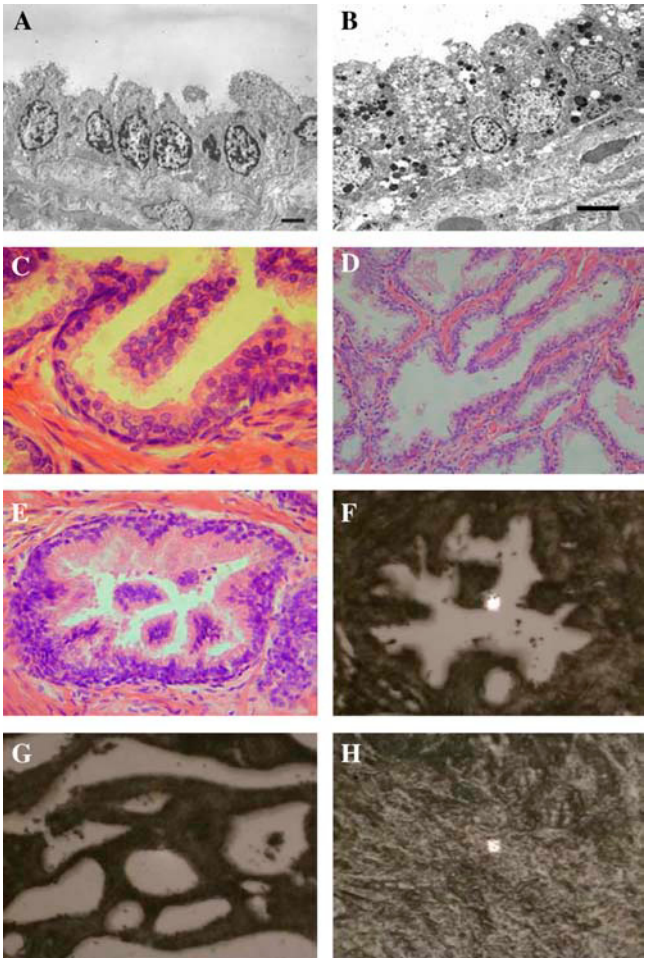

FIGURE 1 Synchrotron FTIR microspectroscopy to interrogate prostate cells (epithelial versus stromal) in situ. Employing electron microscopy and light microscopy, prostatic glandular architecture was noted. Exploiting the phase contrast facility of the Thermo Nicolet continuum microscope, the location of the 10 μm $\times$ 10 μm aperture was tracked. Photomicrographs are of (*A*) electron microscopy of PZ glandular epithelial in cancer-free tissue (PEC4; scale bar = 5 μm); (*B*) electron microscopy of glandular epithelial cells in cancerous tissue (PEC4; scale bar = 10 μm); (*C*) H&E of glandular epithelial cells (PZ) derived from cancer-free tissue (PEC4); (*D*) H&E of glandular elements suspended in stroma (PZ) and derived from cancer-free tissue (PEC4); (*E*) H&E of a TZ glandular element derived from cancer-free tissue (PEC4); (*F*) phase contrast image of a glandular element (TZ) derived from cancer-free tissue (PEC4); (*G*) phase contrast image of glandular elements (TZ) derived from cancerous tissue (PEC4); and (*H*) phase contrast image of stroma (TZ) located in cancer-free tissue (PEC4). Images were obtained by employing conventional methods.

little stromal material (Fig. 1 *D*). Although the TZ often contains markedly fewer glandular elements and large amounts of stromal material, the glandular architecture in this tissue region was similar to that observed in the PZ (Fig. 1 *E*). Exploiting the phase-contrast facility of the Thermo Nicolet Continuum microscope, the 10 μm $\times$ 10 μm aperture was focused along the edge of epithelial cells lining the lumen; in CaP-free glands, spectra were acquired in five separate locations (Fig. 1 *F*). A feature of CaP regions was the presence of small, circular glands; primarily to minimize the possibility of taking more than one spectral reading from the same area, only three separate spectra were acquired from CaP glands (Fig. 1 *G*). Spectral readings ($n = 5$) were also acquired from surrounding stromal material (Fig. 1 *H*).

Epithelial cell spectra

Fig. 2 shows that spectral variation obtained using the $\approx$250 μm $\times$ 250 μm octagon-shaped sampling area of ATR spectroscopy (Fig. 2, *A*, *C*, *E*, *G*, *I*, and *K*) was markedly less than that observed after analysis with the 10 μm $\times$ 10 μm synchrotron IR beam (Fig. 2, *B*, *D*, *F*, *H*, *J*, and *L*). A vibrational spectrum of tissue biochemistry was obtainable from dewaxed sections microtomed from paraffin-embedded blocks although a paraffin band at $\approx$1462 cm^{-1} (in the form of two sharp peaks) remained discernible in some spectra (22). Spectra were normalized to the amide II peak; normalization to the higher-intensity amide I peak tended to exaggeratedly narrow the variability in the spectral region ($\approx$1490–1000 cm^{-1}) containing DNA/RNA. Surprisingly, IR spectra acquired from CaP areas often exhibited less heterogeneity compared to those derived from CaP-free tissue regions (e.g., Fig. 2 *L*). However, upon graphical examination of all the IR spectral data derived from this relatively small cohort number, no discernible tissue region-specific characteristics were readily observable (Fig. 2, *A–L*). Indicating a protein-conformation alteration, a marked shift ($\approx$5 cm^{-1}) in the centroid of the amide I peak of CaP areas ($\approx$1645 cm^{-1}) compared to PZ or TZ regions ($\approx$1640 cm^{-1}) was noted (see Supplementary Material), especially for tissues PEC1, PEC2, PEC3, and PEC4. Previous studies have pointed to marked differences in IR absorbance patterns between $\approx$1000–1200 cm^{-1} (23); this is not readily apparent in our data (Fig. 2, *A–L*).

Stromal spectra

Stroma that surround the glandular elements of a tissue are believed to provide important growth/signaling factors to adjacent epithelial cell populations and are believed to modulate the appropriate functioning of normal cells; likewise, stromal mediators may influence progression and survival of malignant cells (24). Altered function might result in alterations in the spectral signature of CaP stroma compared to cancer free. Individual spectra of prostate CaP stroma after ATR spectroscopy appeared to exhibit markedly less variation compared to those acquired using synchrotron FTIR microspectroscopy (Fig. 3). As observed in the distribution of IR spectra derived from epithelial cells, there was no consistent tissue region-specific trend in this relatively small cohort, i.e., the wavenumber intensities of IR spectra derived from one tissue region were not consistently higher or lower compared to another. Normalization of spectra to the amide II peak highlighted marked intertissue (e.g., Fig. 3 *J*) and intratissue (e.g., Fig. 3 *B*) spectral variation in the DNA/RNA

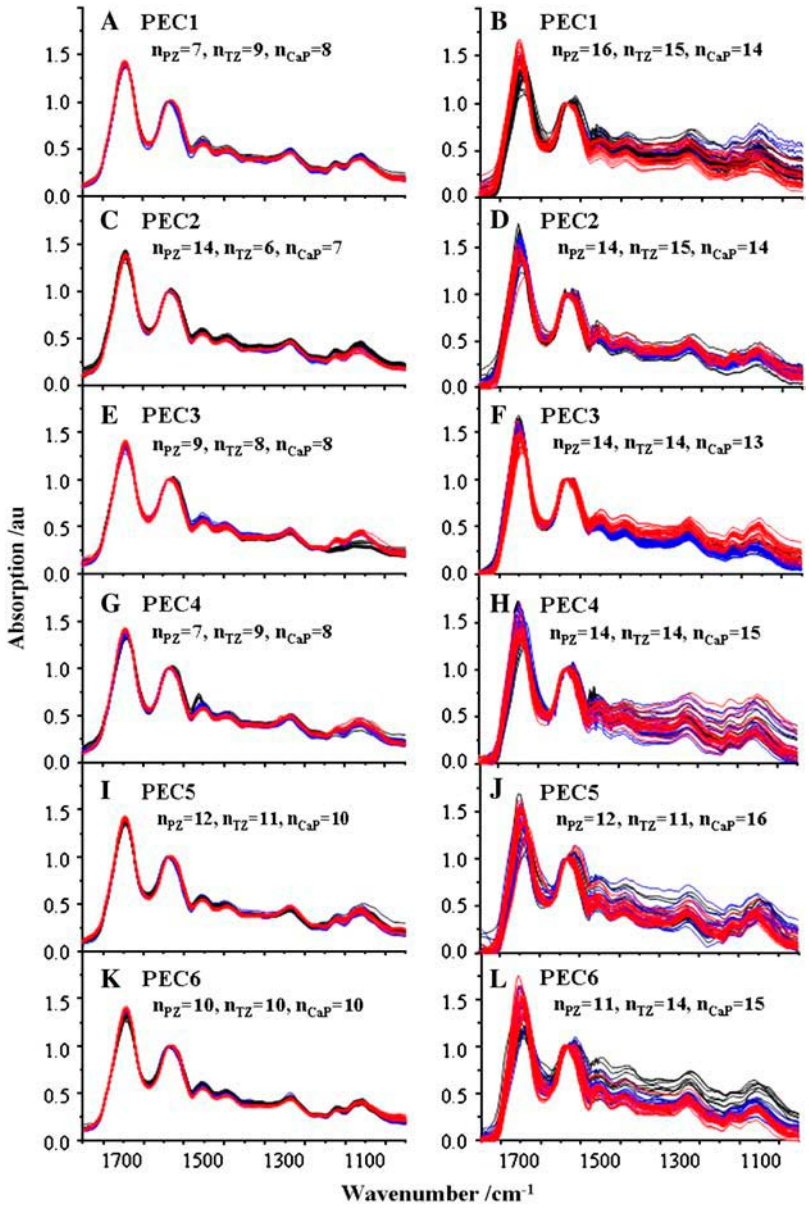

FIGURE 2 Epithelial cell spectra derived from different tissue regions employing either ATR spectroscopy (*A*, *C*, *E*, *G*, *I*, and *K*) or synchrotron FTIR microspectroscopy (*B*, *D*, *F*, *H*, *J*, and *L*). From paraffin-embedded blocks, 10-μm-thick sections were mounted on suitable windows to facilitate IR spectra acquisition before being dewaxed and air dried. Multiple spectra (each from a different location) were acquired from PZ (in *black*), TZ (in *blue*), or CaP (in *red*) regions of prostate tissue sets from six individuals (PEC1–PEC6, as detailed in each panel). Individual spectra were normalized to amide II ($\approx$1533 cm^{-1}).

region of the spectrum. No shift of the centroid of the amide I peak of stroma was observed in any of the tissue sets examined (data not shown).

Spectral differences between tissue regions

After baseline correction and normalization, the spectra were processed as first-derivative (15 points) spectra using Pirouette. First-derivative processing was employed to counter the influence of low frequency effects or dispersion artifacts such as Mie scattering (25). Because 90% of variance was initially associated with minor shifts in amide I (i.e., the most intense peak) and/or amide II, we looked for spectral variation in the region containing DNA/RNA bands ($\approx$1490–1000 cm^{-1}); PCA was conducted on this latter spectral region. Six PCs (in total >90% spectral variation) were selected for analysis (see Supplementary Material), and loadings curves for each PC were plotted for each tissue set (data not shown). These loadings curves allowed the influence of specific spectral features on each PC to be identified; e.g., for four tissue sets, PC1 describes variability in peaks below 1140 cm^{-1}. Scores plots (two-dimensional (2-D)) of each PC pair were then plotted for each tissue set and by combining the clustering evident in these figures (see Supplementary Material) with the analysis of the loadings curves, PCs 1, 2, and 4 were selected as the most appropriate for subsequent three-dimensional (3-D) PCA. Fig. 4, *A* and *C*, shows the median epithelial- and stromal-derived spectra for PZ, TZ, or CaP (PEC1–PEC6) obtained after ATR spectroscopy or synchrotron FTIR microspectroscopy, and Fig.

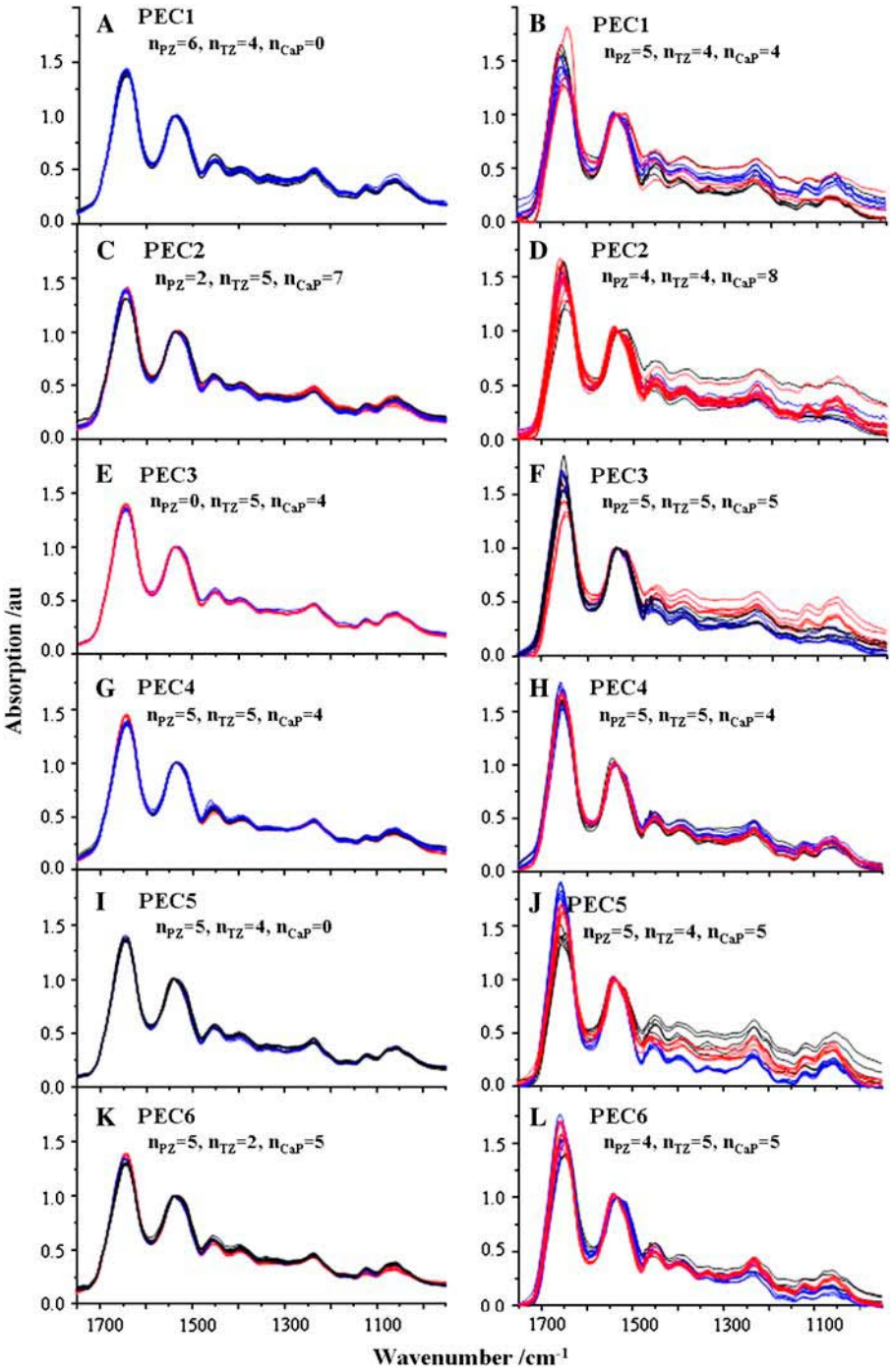

FIGURE 3 Stromal spectra derived from different tissue regions employing either ATR spectroscopy (*A*, *C*, *E*, *G*, *I*, and *K*) or synchrotron FTIR microspectroscopy (*B*, *D*, *F*, *H*, *J*, and *L*). From paraffin-embedded blocks, 10-μm-thick sections were mounted on suitable windows to facilitate IR spectra acquisition before being dewaxed and air dried. Multiple spectra (each from a different location) were acquired from PZ (in *black*), TZ (in *blue*), or CaP (in *red*) regions of prostate tissue sets from six individuals (PEC1–PEC6, as detailed in each panel). Individual spectra were normalized to amide II (≈1533 cm^{-1}).

4, *B* and *D*, shows the corresponding cluster vectors plotted to highlight spectral variation in the DNA/RNA region. Comparing the median spectra, subtle differences between all three tissue regions (PZ, TZ, or CaP) were observed throughout the spectral region (950–1750 cm^{-1}) (Fig. 4, *A* and *C*). Interestingly, the most marked spectral differences between the different tissue regions were observed in the ≈1000 cm^{-1} to ≈1200 cm^{-1} region after synchrotron FTIR microspectroscopic analysis of CaP stroma compared to PZ or TZ stroma (23). Although the use of first-derivative processing would be expected to remove low amplitude baseline variations due to dispersion artifacts, as a consequence of the size of the cells (≈20 μm × 20 μm) with respect to the aperture, a number of the spectra may have been taken from areas that contained cellular edges; this could still give rise to dispersion artifacts in the acquired spectra. An analysis of positive and negative loadings (the intensity of each equally important) using cluster vectors

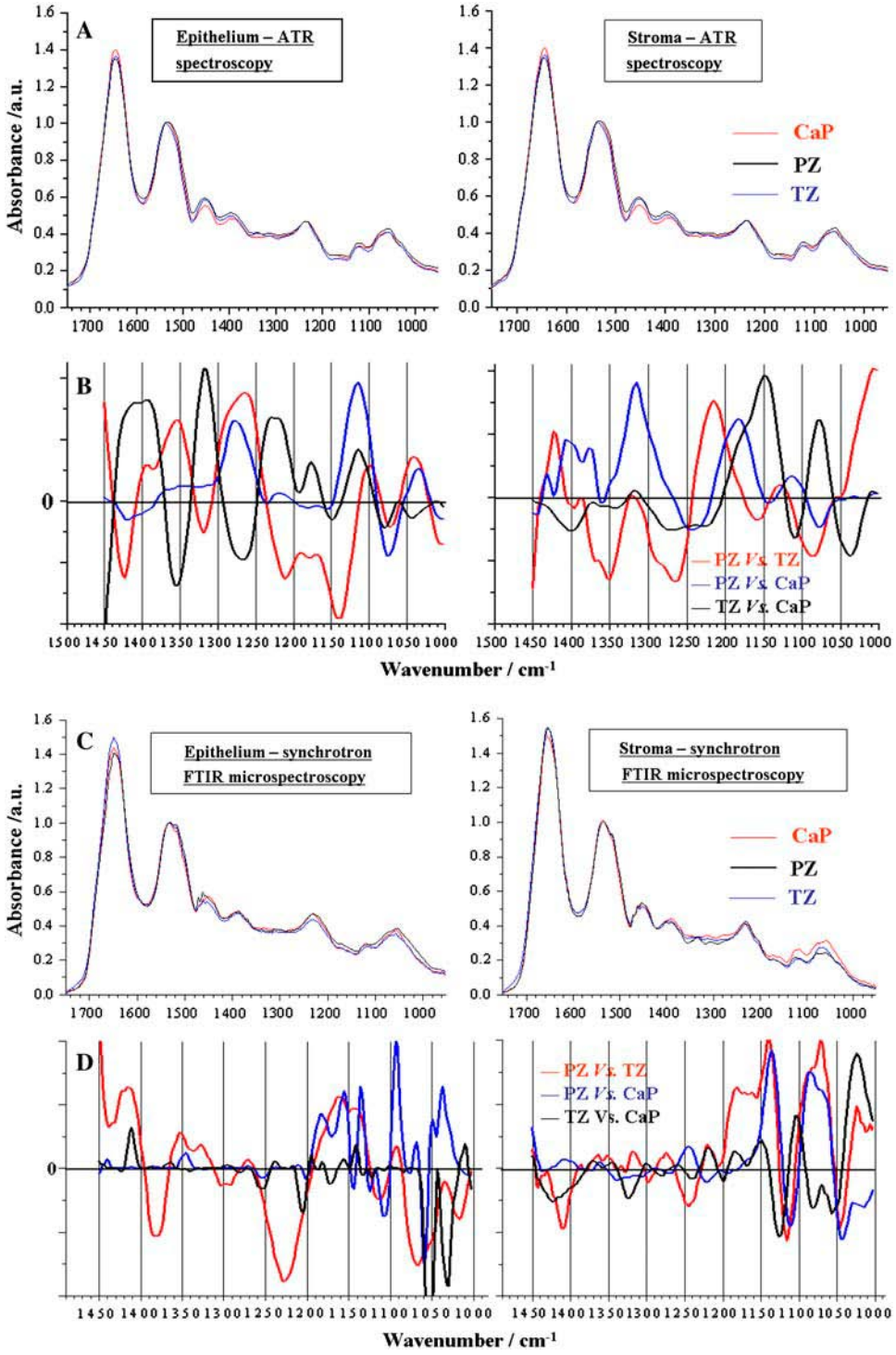

FIGURE 4 Median spectra (*A* and *C*) and cluster vectors (*B* and *D*) for all spectra acquired either from epithelial cells lining glandular elements or stroma after ATR spectroscopy or synchrotron FTIR microspectroscopy. Spectra were collected and medians were derived from all the spectra acquired for a particular tissue region (PZ, *black line*; TZ, *blue line*; and CaP, *red line*). Cluster vectors examining loadings as a function of wavenumber were plotted as described (see Supplementary Material).

(Fig. 4, *B* and *D*) suggested that after ATR spectroscopy, variance was detectable when comparing either epithelial- or stromal-derived spectra of different tissue regions (PZ versus TZ, PZ versus CaP, or TZ versus CaP) throughout the ≈1490–1000 cm^{-1} spectral region examined, whereas synchrotron FTIR microspectroscopic variance appeared to be mostly confined to the ≈1000–1200 cm^{-1} region (Table 2). With ATR spectroscopy, the majority of variability occurred at the wavenumbers ≈1430 cm^{-1}, ≈1400 cm^{-1}, ≈1360–1280 cm^{-1}, ≈1225 cm^{-1}, and ≈1185–1120 cm^{-1}, along with others <≈1100 cm^{-1}. Except for ≈1430 cm^{-1}, the majority of the variability detected using synchrotron FTIR microspectroscopy was <≈1200 cm^{-1} (Table 2). The tissues that appeared most dissimilar when analyzed by this

TABLE 2 Loadings (or variance) as a function of wavenumber derived from cluster vectors

	ATR spectroscopy						Synchrotron FTIR microspectroscopy					
	PZ versus TZ		PZ versus CaP		TZ versus CaP		PZ versus TZ		PZ versus CaP		TZ versus CaP	
Wavenumber (cm^{-1}), assignation	E	S	E	S	E	S	E	S	E	S	E	S
≈1430, the conformationally sensitive αMethylene γCH_2	√	√		√	√		√	√			√	√
≈1400, COO^- symmetric stretching vibrations of fatty acids and amino acids	√	√		√	√	√						
≈1370, methyl symmetric bends ($_s\gamma CH_3$)		√		√			√					
≈1360–1280, amide III absorptions (predominantly C-N stretching) with significant contributions from CH_2 stretching vibrations of carbohydrate residues	√		√	√	√	√	√					
≈1350–1260, PO_2^- antisymmetric stretch ($_{as}\nu PO_2^-$)		√			√		√					
≈1240				√				√		√		
≈1225, PO_2^- asymmetric stretching vibrations of nucleic acids and phospholipids		√			√	√	√					
≈1215	√											
≈1185–1120, C-O ring vibrations of nucleic acid ''sugars''	√		√		√	√	√	√	√			
≈1160		√						√	√			
≈1140, C-O stretch (ν_{CO})	√		√						√	√		
≈1100, C-O stretch (ν_{CO})	√											
≈1090–1060								√	√	√		
≈1084, PO_2^- symmetric stretching vibrations of nucleic acids and phospholipids		√		√		√	√		√	√		√
≈1070	√		√	√			√		√	√		√
≈1050											√	√
≈1040, C-O stretch (ν_{CO})	√					√	√	√	√	√		
≈1030–1020	√	√	√				√	√	√	√	√	√

√, variance observed in this tissue comparison; E, epithelial; S, stromal.

method were epithelial cells of the PZ compared to those located in the TZ. Conversely, the most similar cell types appeared to be epithelial cells located in the TZ compared to those in CaP regions (Table 2).

Identification of clusters using principal component analysis

PCA (3-D) of epithelial cell spectra was performed to determine if segregation of different tissue regions might be achieved along chosen PCs (1, 2, and 4) and whether rotated data might point to similarities or differences. Using these three PCs it proved possible to obtain segregated clustering for cancer-free and CaP regions with all tissue sets except PEC4 (Fig. 5). Spectra derived from this tissue set did not exhibit any significant clustering; the example shown in Fig. 5 *D* uses PCs 3, 4, and 6. Fig. 5, *A–F*, shows 3-D scores plots for PEC1–PEC6, respectively, after analyses using synchrotron FTIR microspectroscopy (for scores plots acquired using ATR spectroscopy, see Supplementary Material). In the main, cell spectra from the different tissue regions (PZ, TZ, or CaP) formed clusters. Nearness in multivariate distance implies spectral similarity, and separation in the 3-D plots signifies spectral differences. In general, there was good separation between CaP-free tissues (PZ or TZ) and CaP pointing to the potential of multivariate analysis of IR spectra to segregate different cell types of the prostate. Somewhat surprisingly, in two cases (PEC3 (Fig. 5 *C*) and PEC6 (Fig. 5 *F*)) TZ-derived spectral scores seem to be more closely aligned to CaP spectra. However, in this relatively small patient cohort ($n = 6$) such observations may not be indicative of a general occurrence; this would need to be tested in a population-based study.

Carbohydrate/phosphate ratio versus RNA/DNA ratio

A number of measures of cellular metabolic status were obtainable even after paraffin-embedding and dewaxing; these may be potential diagnostic indicators (13,26,27). An examination of such spectrally derived biomarkers for epithelial cells revealed marked intra- and inter-individual differences when carbohydrate/phosphate ratio was plotted against RNA/DNA ratio (Fig. 6). Higher RNA/DNA ratio is associated with increasing malignancy (26) as are lower carbohydrate and phosphate levels (28). Spectra derived after synchrotron FTIR microspectroscopy pointed to PZ epithelial cells having higher carbohydrate/phosphate ratios

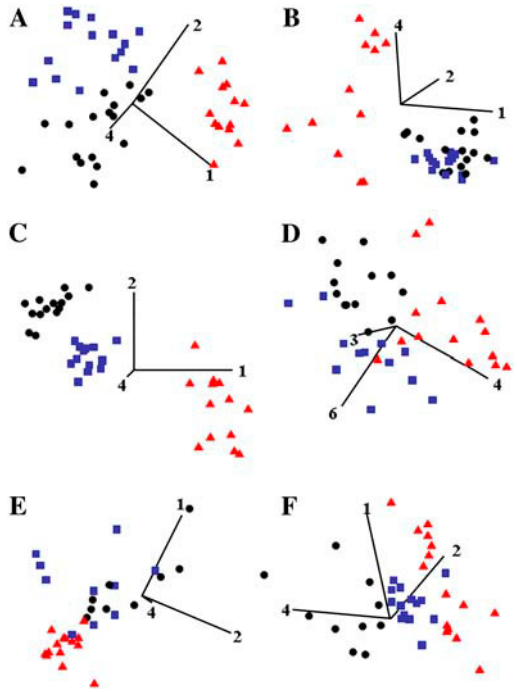

FIGURE 5 3-D scores plots on PCs selected to demonstrate best segregation of epithelial cell spectra derived from the different tissue regions. Spectra were collected using synchrotron FTIR microspectroscopy. Each spectrum for each tissue region (PZ, *black circles*; TZ, *blue squares*; CaP, *red triangles*) was expressed in terms of chosen PCs using Pirouette software and rotated to identify segregation of different clusters. Each symbol represents a single spectrum as a single point in ''hyperspace''. The 3-D scores plots represent the following: (*A*) PEC1 on PC1, PC2, and PC4; (*B*) PEC2 on PC1, PC4, and PC5; (*C*) PEC3 on PC1, PC2, and PC6; (*D*) PEC4 on PC2, PC3, and PC4; (*E*) PEC5 on PC2, PC3, and PC5; and (*F*) PEC6 on PC1, PC4, and PC5.

and lower RNA/DNA ratios (Fig. 6 *A*) with CaP cells having the opposite, lower carbohydrate/phosphate ratios and higher RNA/DNA ratios (Fig. 6 *C*). TZ epithelial cells appeared to exhibit intermediate levels of these biomarkers (Fig. 6 *B*).

PZ versus TZ cryosections of unfixed tissue

From a CaP-free prostate obtained after cystoprostatectomy, isolated PZ and TZ tissue slices were snap frozen within 10 min of surgical resection. The value of this tissue was that it allowed an IR interrogation of different tissue regions within a CaP-free organ; cryosections from snap-frozen tissues were analyzed to allow for spectral comparisons with dewaxed paraffin-embedded sections previously used. PZ and TZ epithelial cell spectra were obtained using synchrotron FTIR microspectroscopic analysis of 10-μm-thick cryosections on BaF_2 windows. PZ epithelial cell spectra appeared to be tightly grouped, whereas those of the TZ exhibited marked variations in wavenumber intensities (see Supplementary Material). This gave rise to very apparent differences in median spectra acquired from the two tissue regions (Fig. 7 *A*). A peak in wavenumber intensity was observable in both tissue-specific spectra between the $\approx$1700–1750 cm^{-1} region and this may be associated with C=O stretching vibrations of lipids (1740 cm^{-1}). It appeared to be more pronounced in PZ compared to TZ and these wavenumber intensities were not observed in the dewaxed tissue sections (PEC1–PEC6). There were also marked differences in the spectral region ($\approx$1490–1000 cm^{-1}) containing DNA/RNA with median intensity elevations in glycoproteins ($\approx$1380 cm^{-1}), amide III ($\approx$1260 cm^{-1}), and carbohydrates ($\approx$1155 cm^{-1}) being associated with PZ epithelial cell spectra compared to TZ (Fig. 7 *A*). However, the most marked changes in the pattern of IR absorbance occurred between $\approx$1000–1200 cm^{-1}. Based on the aforementioned spectral attributions, these spectral differences (many associated with structural alterations in nucleic acids) translated into strong cluster separation between PZ and TZ scores in 3-D plots along PCs 1, 2, and 3 (Fig. 7 *B*). It is interesting to note that no overlap in epithelial cell clusters derived from either of the two tissue regions was observed. This points to marked biomolecular and/or conformational differences between epithelial cells located in these two tissue regions of the human prostate (Fig. 7 *B*).

DISCUSSION

Prostate tissue consists of branched tubuloacinar glands embedded in a fibromuscular stroma. It is a hormone-responsive organ divided into the TZ (surrounds the urethra, $\approx$5% of normal organ volume), the CZ (surrounds the ejaculatory ducts, $\approx$20% of normal organ volume), and the PZ (contains the bulk of glandular tissue, $\approx$75% of normal organ volume) (1,2). Androgens are believed to stimulate prostatic growth and secretory functions, whereas estrogens are believed to act as growth inhibitors (29). Within the gland there appears to be a zone-specific susceptibility to malignancy, in that CaP rarely originates in the CZ but occurs mostly in the PZ and to a lesser degree in the TZ (3). This apparent tissue-specific resistance to the progression of invasive carcinoma is shared by adjacent reproductive organs such as the vas deferens, epididymis, and seminal vesicles (30). BPH, a nonmalignant overgrowth of the epithelial and fibromuscular tissues, is mainly confined to the TZ (3,31). Given the high incidence of CaP, especially in an ageing population, there is an urgent need to develop a biomarker approach to monitor and identify individuals at risk of progression to invasive disease. By comparing IR spectra derived from 10-μm-thick sections of PZ, TZ, or CaP, we set out to determine whether it was possible to identify potential biomarkers of susceptibility in the CaP-susceptible region.

CaP incidence is increasing steadily in most countries worldwide (6), yet its etiology remains obscure (10). Environmental agents that might induce genomic damage (32) or proliferative stimuli (33) might play a key role in initiation and/or promotion of this disease. Age-related structural changes (e.g., 8-hydroxypurine lesions) give rise to a DNA phenotype in nonmalignant prostate tissues of older men

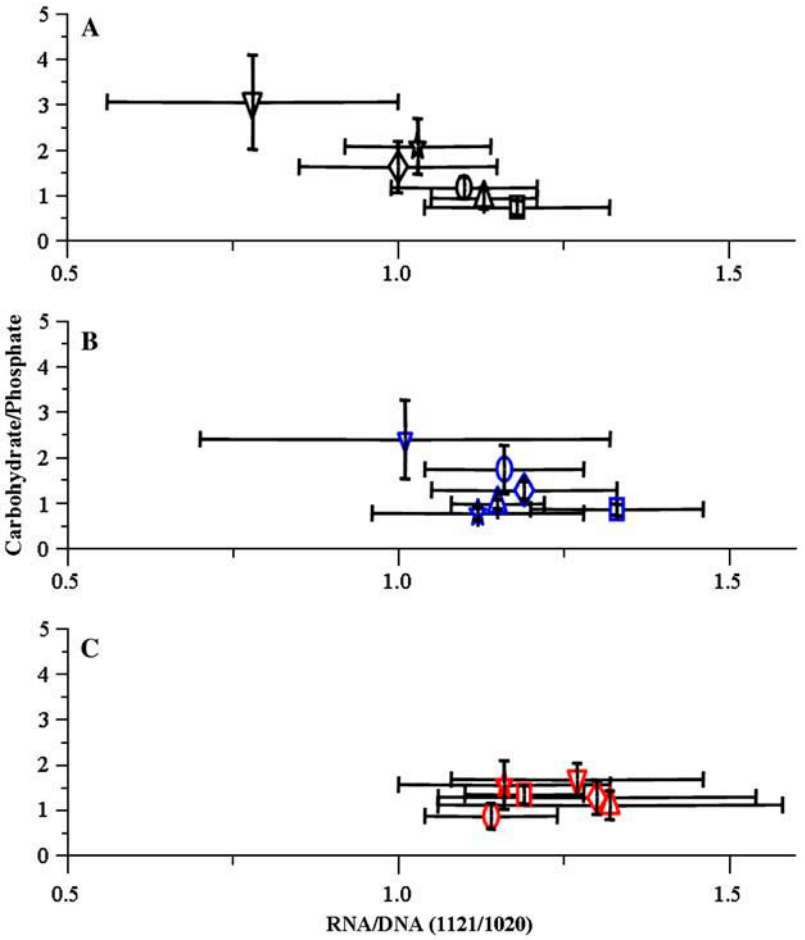

FIGURE 6 2-D plots of the ratios for carbohydrate (quantified by the integrated absorbance in the 900–1185 cm^{-1} region) to phosphates of nucleic acids (quantified by the integrated absorbance in the 1185–1300 cm^{-1} region) versus RNA/DNA (based on the intensity at wavenumber 1121 cm^{-1}/intensity at 1020 cm^{-1}). Each symbol represents the mean ± SD of all the spectrally derived estimations for one tissue region (PZ, TZ, or CaP). The 2-D plots represent the following: (*A*) spectrally derived estimations for PZ; (*B*) spectrally derived estimations for TZ; and (*C*) spectrally derived estimations for CaP. These estimations were derived using OPUS software.

(aged 55–80 y) with features similar to primary CaP (34). In normal prostate, a metastatic CaP DNA phenotype also occurs that shares structural similarities to DNA isolated from metastasizing tumors; this exhibits a distinctly different conformation compared to the primary CaP phenotype (35). Structural modifications of phosphodiester-deoxyribose that accompany mutagenic base changes may be a result of environmental exposure to chemicals (36) but are more likely to be the result of subsequent events (e.g., oxidative damage) that accelerate genomic instability and consequently result in additional mutagenic damage (37). This is powerful evidence supporting the use of IR spectroscopy to identify biomarkers of CaP progression.

We employed two spectroscopic methods (ATR spectroscopy and synchrotron FTIR microspectroscopy) to rigorously interrogate prostate tissue sets consisting of CaP-free PZ, CaP-free TZ, and CaP isolated from a cohort of men ($n = 7$) aged 58–68 y (Table 1). ATR spectroscopy acquired spectra within a ≈250 μm × 250 μm octagon-shaped sampling area, whereas a 10 μm × 10 μm aperture was used for synchrotron FTIR microspectroscopic analyses. Although the effective depth of the evanescent wave in ATR spectroscopy may vary with wavenumber, this technique is very comparable to a transmission measurement and, given that tissue sections analyzed in this study were at most 10-μm thick, we would expect that representative spectra were obtained from our samples. Nevertheless, both techniques highlighted similar spectral characteristics, despite the fact that spectra obtained after ATR spectroscopy exhibited markedly less variability compared to the high degree of intratissue variability often observed after synchrotron FTIR microspectroscopy (Figs. 1 and 2, see Supplementary Material). The reason may be that with ATR spectroscopy, the bigger sampling area results in an averaging of spectral signatures of tens of cells, depending on the positioning of the crystal. In contrast, a method such as synchrotron FTIR microspectroscopy may interrogate an individual ≈10 μm × 10 μm epithelial or stromal cell. This averaging effect with ATR spectroscopy would have the advantage of delivering a biochemical cell signature over a wider surface area. A disadvantage would be that a signature unique to a particular cell type might be lost in such an averaged spectrum and for this purpose, synchrotron FTIR microspectroscopy might be employed to facilitate single-cell interrogation. However, it is of note that 3-D scores plots examining the clustering of individual tissue-derived spectra do point to comparable

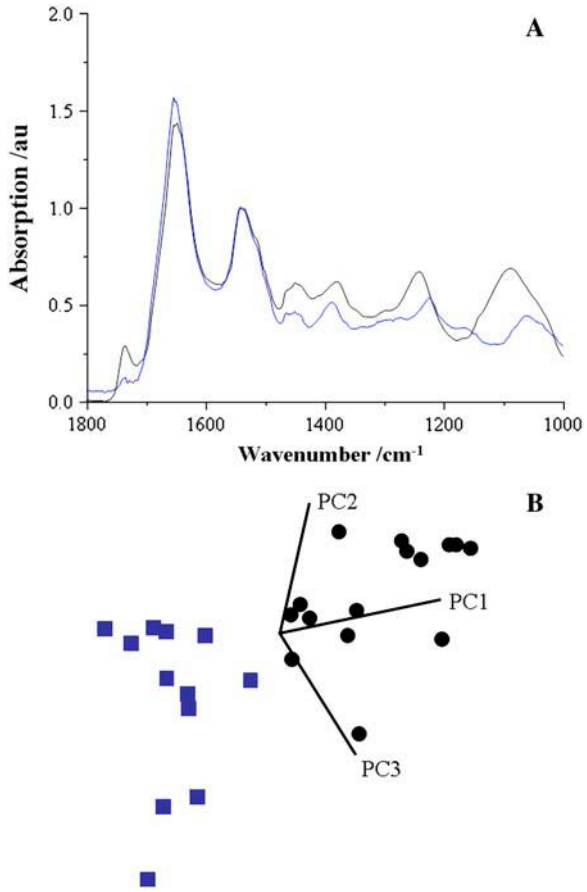

FIGURE 7 Median spectra and 3-D scores plots on PCs selected to demonstrate segregation of spectra derived from epithelial cells of PZ versus TZ isolated from a cystoprostatectomy specimen (PEC7). Spectra were collected using synchrotron FTIR microspectroscopy, and medians were derived from all the spectra acquired for a particular tissue region (PZ, *black line*; TZ, *blue line*). Each spectrum for each tissue region (PZ, *black circles* TZ, *blue squares*) were expressed in terms of chosen PCs using the Pirouette software and rotated to identify segregation of different clusters.

findings from both methods (Fig. 5, see Supplementary Material). For instance, using both techniques, spectra from all three tissue regions (PZ, TZ, or CaP) of PEC1 show good clustering compared to those of PEC3 that suggest a closer alignment of TZ-derived spectra to CaP, whereas those of PEC6 point to a strong similarity between PZ and TZ but a segregation of both from CaP. In this relatively small patient cohort, no consistent clustering effects were observed, suggesting that inter-individual variation in biochemistry may outweigh the potential to identify specific biomarkers within this pilot study.

A molecular mechanism for region-specific susceptibility to different pathologies in the prostate remains obscure. One possible explanation may be that the urogenital sinus is the tissue of origin for most of the prostate gland including the PZ and TZ, whereas regions that remain relatively free of disease arise from the mesonepheric duct, e.g., the CZ (1). This would suggest that epithelial cells of different regions that differ in their embryonic origin also differ in their susceptibility to pathological stimuli. Another explanation might be the presence of region-specific hormonal and growth factor influences that might serve to modulate disease progression. Higher levels of epidermal growth factor, testosterone, and dihydrotestosterone in the periurethral (TZ) region compared to the subcapsular (PZ) region of the prostate might explain region-specific BPH development (38). Immunohistochemical (IHC) analysis for π-class glutathione-*S*-transferase (GST), an important detoxification enzyme, in TZ and PZ high-grade prostatic intraepithelial neoplasia (PIN) showed that GST π was present in TZ PIN but was absent in PZ PIN (39). Further IHC analysis for estrogen receptors showed that atrophic changes of PZ were more immunoreactive than hyperplastic lesions of TZ (40). Tissue regional differences in stromal components may also occur. A decrease in smooth muscle cells and an increase in collagen fibers may occur in the PZ compared to TZ (41). Finally, the hormone- and/or carcinogen-metabolizing capacity of epithelial cells residing in different zones might differ (3). This may further influence their viability, especially in response to sex steroid addition, e.g., PZ epithelial cells more viable compared to TZ (42).

The cluster vectors are from the 0,0 of 3-D hyperspace and so may not give a direct comparison of the variance between the median spectra of one cluster and another but our novel approach, as opposed to examining the loadings curves of each PC in turn, does give a better idea of where the variance lies. An examination of the spectral variance between PZ, TZ, or CaP regions suggests that PZ versus TZ epithelial cell spectra exhibit differences throughout the $\approx$1490–1000 cm^{-1} region after interrogation with either IR spectroscopy technique (Fig. 4, *B* and *D*, Table 2). This suggests that significant differences do exist in the biochemistry of prostate epithelial cells depending on whether they reside in the TZ or PZ and is of great importance for future studies that will set out to identify the relative importance of these potential biomarkers. For instance, a more intense wavenumber peak that might be associated with increased lipid content may point to increased hormone responsiveness in the PZ compared to the TZ (Fig. 7 *A*). A tissue (micro)environment containing higher hormone levels may act as a driver for the progression of CaP (3). Such observations would support the notion of an underlying biochemistry for an enhanced susceptibility to adenocarcinoma in PZ epithelial cells compared to TZ. However, fewer epithelial cell spectral differences were observed when comparing TZ versus CaP as opposed to PZ versus CaP (Fig. 4 *D*) and if these occurred, they were localized between $\approx$1000–1200 cm^{-1}.

Our observations are surprising because one might reasonably expect that the apparently more susceptible (i.e., to adenocarcinoma) PZ epithelial cells would be spectrally more similar to CaP. However, further support for our finding is that PZ epithelial cells have higher carbohydrate/phosphate ratios and lower RNA/DNA ratios compared to CaP cells, whereas those of the TZ exhibit intermediate

levels (Fig. 6). Although ATR spectroscopy suggests that marked differences exist between TZ versus CaP, this variance is markedly localized after synchrotron FTIR microspectroscopy (Table 2). This spectrally derived biochemical information again suggests that TZ epithelial cells are more similar to CaP. Because of the larger sampling area involved in ATR spectroscopy, acquired spectra may not be totally epithelial cell derived. However, synchrotron FTIR microspectroscopy allows for the direct focusing of the IR beam on target cells of interest. Future plans for the development of a methodology for high resolution IR analysis will involve a recently established microspectroscopic technique, known as photothermal microspectroscopy (PTMS) (14). PTMS allows the acquisition of subcellular spatial resolution without the need to involve the elaborate and costly synchrotron facilities.

The TZ is the region where most pathology (i.e., BPH and 25% CaP) occurs in the human prostate, and it is not inconceivable that a zone-specific factor (i.e., hormonal) might be an important driver in CaP progression. It is possible that our studies using IR spectroscopy have picked up biochemical alterations such as initiating events to which epithelial cells of the TZ are as susceptible, if not more so, as those of the PZ. However, in the absence of a putative stimulus (e.g., hormone exposure) such initiated cells may not progress into invasive CaP. In a tissue region that may receive fewer mutation hits but contain a far greater number of potential targets (i.e., epithelial cells of glandular elements), the presence of a growth-promoting effect may be an important risk factor. Although observed in a small patient number, our results might explain the excess of nonmalignant overgrowth in the TZ, i.e., initiating events may occur to give rise to a CaP-like phenotype but in the absence of a suitable stimulus these initiated cells do not progress to CaP.

Our study and others (13,23,26,27,34,35,37) point to the realistic possibility of employing archival material (e.g., paraffin-embedded tissue blocks, frozen tissues) to investigate spectral alterations associated with disease progression and to link these observations with susceptibility, biochemical influences, and diagnostic/prognostic indicators. The ability of IR spectroscopy to sensitively monitor metabolic processes in tissues or cells does provide important structural information (43). The elucidation of tissue-specific susceptibility remains an important challenge, and the use of spectroscopic methods may be an important tool to investigate this, especially in retrospective studies where findings may be linked to individual details or prognostic outcome. Surprisingly, although our findings point to the ability of IR spectroscopy with multivariate analysis to segregate different cell types of the prostate, it appears in the tissues we examined that TZ epithelial cells possess a more similar biochemical cell spectral fingerprint to CaP compared to those in the apparently more susceptible PZ region. The role of underlying growth-promoting effects that might accelerate transformation in the prostate requires urgent attention.

CONCLUSIONS

Spectrally designated structural characteristics allow, with PCA, the segregation of spectral scores derived from different regions (PZ, TZ, and/or CaP) of the prostate. As detected by synchrotron FTIR microspectroscopy with its powerful ability to target individual cells, differences between epithelium of the TZ versus CaP are markedly fewer compared to PZ versus CaP. The prostate tissue regions that were most dissimilar are PZ versus TZ. PZ exhibits a higher occurrence of CaP, so other mechanisms (e.g., hormone exposure) may modulate the growth kinetics of initiated epithelial cells in this tissue region. Otherwise, because the PZ contains a far greater number of potential targets (i.e., epithelial cells) for mutation hits, it may be at a greater risk. For the development of IR spectroscopy as a monitoring and/or diagnostic tool, future work will require the interrogation of large patient cohorts to build a database of normal versus abnormal biochemical cell spectral fingerprints to eliminate confounding factors such as interindividual variation.

SUPPLEMENTARY MATERIAL

An online supplement to this article can be found by visiting BJ Online at http://www.biophysj.org.

We thank John M. Chalmers (VS Consulting) for helpful discussions.

This work was funded by an Engineering and Physical Sciences Research Council grant GR/S75918/01 (M.J.G., A.H., N.J.F., F.L.M., and H.M.P.) and the Rosemere Cancer Foundation (N.R., S.S.M., and A.C.H.).

REFERENCES

1. McNeal, J. E. 1988. Normal histology of the prostate. *Am. J. Surg. Pathol.* 12:619–633.
2. McNeal, J. E. 1988. The prostate gland: morphology and pathobiology. *Monograph Urol.* 9:36–63.
3. Ragavan, N., R. Hewitt, L. J. Cooper, K. M. Ashton, A. C. Hindley, C. M. Nicholson, N. J. Fullwood, S. S. Matanhelia, and F. L. Martin. 2004. CYP1B1 expression in prostate is higher in the peripheral than in the transition zone. *Cancer Lett.* 215:69–78.
4. Office for National Statistics. 1996. Mortality Statistics by Cause: England and Wales 1996. Series DH2, No. 23. Her Majesty's Stationary Office, London, UK.
5. American Cancer Society. 1991. Cancer Facts and Figures—1991. ACS, Atlanta, GA.
6. Grönberg, H. 2003. Prostate cancer epidemiology. *Lancet.* 361:859–864.
7. Troyer, D. A., J. Mubiru, R. J. Leach, and S. L. Naylor. 2004. Promise and challenge: markers of prostate cancer detection, diagnosis and prognosis. *Dis. Markers.* 20:117–128.
8. Karayi, M. K., D. E. Neal, and A. F. Markham. 2000. Current status of linkage studies in hereditary prostate cancer. *BJU Int.* 86:659–669.
9. Kolonel, L. N., D. Altshuler, and B. E. Henderson. 2004. The multiethnic cohort study: exploring genes, lifestyle and cancer risk. *Nat. Rev. Cancer.* 4:519–527.
10. Grover, P. L., and F. L. Martin. 2002. The initiation of breast and prostate cancer. *Carcinogenesis.* 23:1095–1102.
11. Parkin, D. M., F. I. Bray, and S. S. Devesa. 2001. Cancer burden in the year 2000. The global picture. *Eur. J. Cancer.* 37(Suppl. 8):S4–S66.

12. Dunsmuir, W. D., D. Hrouda, and R. S. Kirby. 1998. Malignant changes in the prostate with ageing. *Br. J. Urol.* 82(Suppl. 1):47–58.

13. Argov, S., R. K. Sahu, E. Bernshtain, A. Salman, G. Shohat, U. Zelig, and S. Mordechai. 2004. Inflammatory bowel diseases as an intermediate stage between normal and cancer: a FTIR-microspectroscopy approach. *Biopolymers.* 75:384–392.

14. Hammiche, A., M. J. German, R. Hewitt, H. M. Pollock, and F. L. Martin. 2005. Monitoring cell cycle distributions in MCF-7 cells using near-field photothermal microspectroscopy. *Biophys. J.* 88:3699–3706.

15. Holman, H. N., M. C. Martin, E. A. Blakely, K. Bjornstad, and W. R. McKinney. 2000. IR spectroscopic characteristics of cell-cycle and cell death probed by synchrotron radiation based Fourier transform IR spectroscopy. *Biopolymers.* 57:329–335.

16. Mantsch, H. H., and M. Jackson. 1996. *In* Infrared Spectroscopy of Biomolecules. Wiley-Liss, New York.

17. Mourant, J. R., Y. R. Yamada, S. Carpenter, L. R. Dominique, and J. P. Freyer. 2003. FTIR spectroscopy demonstrates biochemical differences in mammalian cell cultures at different growth stages. *Biophys. J.* 85: 1938–1947.

18. Gazi, E., J. Dwyer, N. P. Lockyer, J. Miyan, P. Gardner, C. Hart, M. Brown, and N. W. Clarke. 2005. Fixation protocols for subcellular imaging by synchrotron-based Fourier transform infrared microspectroscopy. *Biopolymers.* 77:18–30.

19. Tobin, M. J., M. A. Chesters, J. M. Chalmers, F. J. M. Rutten, S. E. Fisher, I. M. Symonds, A. Hitchcock, R. Allibone, and S. Dias-Gunasekara. 2004. Infrared microscopy of epithelial cancer cells in whole tissues and in tissue culture, using synchrotron radiation. *Faraday Discuss.* 126:27–39.

20. Davies, A. M. C., and T. Fearn. 2004. Back to basics: the principles of principal component analysis. *Spectroscopy Europe.* 16:20–23.

21. Busch, C., T. A. Hanssen, C. Wagener, and B. Öbrink. 2002. Down-regulation of CEACAM1 in human prostate cancer: correlation with loss of cell polarity, increased proliferation rate, and Gleason grade 3 to 4 transition. *Hum. Pathol.* 33:290–298.

22. Fernandez, D. C., R. Bhargava, S. M. Hewitt, and I. W. Levin. 2005. Infrared spectroscopic imaging for histopathologic recognition. *Nat. Biotechnol.* 23:469–474.

23. Gazi, E., P. Gardner, A. Ghanbari-Siahkali, A. P. Wade, J. Miyan, N. P. Lockyer, J. C. Vickerman, N. W. Clarke, J. H. Shanks, L. J. Scott, C. A. Hart, and M. Brown. 2003. Applications of Fourier transform infrared microspectroscopy in studies of benign prostate and prostate cancer. A pilot study. *J. Pathol.* 201:99–108.

24. Yang, F., J. A. Tuxhorn, S. J. Ressler, S. J. McAlhany, T. D. Dang, and D. R. Rowley. 2005. Stromal expression of connective tissue growth factor promotes angiogenesis and prostate cancer tumorigenesis. *Cancer Res.* 65:8887–8895.

25. Mohlenhoff, B., M. Romeo, M. Diem, and B. R. Wood. 2005. Mie-type scattering and non-Beer-Lambert absorption behavior of human cells in infrared microspectroscopy. *Biophys. J.* 88:3635–3640.

26. Argov, S., J. R. A. Salman, I. S. J. Goldstein, H. Guterman, and S. Mordechai. 2002. Diagnostic potential of Fourier-transform infrared microspectroscopy and advanced computational methods in colon cancer patients. *J. Biomed. Opt.* 9:558–567.

27. Mordechai, S., R. K. Sahu, Z. Hammody, S. Mark, K. Kantarovich, H. Guterman, A. Podshyvalov, J. Goldstein, and S. Argov. 2003. Possible common biomarkers from FTIR microspectroscopy of cervical cancer and melanoma. *J. Microsc.* 215:86–91.

28. Cohenford, M. A., and B. Rigas. 1998. Cytologically normal cells from neoplastic cervical samples display extensive structural abnormalities on IR spectroscopy: implications for tumor biology. *Proc. Natl. Acad. Sci. USA.* 95:15327–15332.

29. Risbridger, G. P., J. J. Bianco, S. J. Ellem, and S. J. McPherson. 2003. Oestrogens and prostate cancer. *Endocr. Relat. Cancer.* 10:187–191.

30. Coffey, D. S. 2001. Similarities of prostate and breast cancer: evolution, diet, and estrogens. *Urology.* 57(Suppl. 4A):31–38.

31. Li, M. J., H. S. Hsu, R. C. Liang, and S. Y. Lin. 2002. Infrared microspectroscopic detection of epithelial and stromal growth in the human benign prostatic hyperplasia. *Ultrastruct. Pathol.* 26:365–370.

32. Rybicki, B. A., A. Rundle, A. T. Savera, S. S. Sankey, and D. Tang. 2004. Polycyclic aromatic hydrocarbon-DNA adducts in prostate cancer. *Cancer Res.* 64:8854–8859.

33. Timms, B. G., K. L. Howdeshell, L. Barton, S. Bradley, C. A. Richter, and F. S. vom Saal. 2005. Estrogenic chemicals in plastic and oral contraceptives disrupt development of the fetal mouse prostate and urethra. *Proc. Natl. Acad. Sci. USA.* 102:7014–7019.

34. Malins, D. C., P. M. Johnson, E. A. Barker, N. L. Polissar, T. M. Wheeler, and K. M. Anderson. 2003. Cancer-related changes in prostate DNA as men age and early identification of metastasis in primary prostate tumors. *Proc. Natl. Acad. Sci. USA.* 100:5401–5406.

35. Malins, D. C., N. K. Gilman, V. M. Green, T. M. Wheeler, E. A. Barker, M. A. Vinson, M. Sayeeduddin, K. E. Hellström, and K. M. Anderson. 2004. Metastatic cancer DNA phenotype identified in normal tissues surrounding metastasizing prostate carcinomas. *Proc. Natl. Acad. Sci. USA.* 101:11428–11431.

36. Malins, D. C., N. L. Polissar, and S. J. Gunselman. 1997. Infrared spectral models demonstrate that exposure to environmental chemicals leads to new forms of DNA. *Proc. Natl. Acad. Sci. USA.* 94:3611–3615.

37. Malins, D. C., N. L. Polissar, and S. J. Gunselman. 1997. Tumor progression to the metastatic state involves structural modification in DNA markedly different from those associated with primary tumor formation. *Proc. Natl. Acad. Sci. USA.* 93:14047–14052.

38. Sciarra, F., S. Monti, M. V. Adamo, E. Palma, V. Toscano, G. d'Eramo, and F. di Silverio. 1995. Regional distribution of epidermal growth factor, testosterone and dihydrotestosterone in benign prostate hyperplasia tissue. *Urol. Res.* 23:387–390.

39. Montironi, R., R. Mazzucchelli, D. Stramazzotti, R. Pomante, D. Thompson, and P. H. Bartels. 2000. Expression of π-class glutathione S-transferase: two populations of high grade prostatic intraepithelial neoplasia with different relations to carcinoma. *Mol. Pathol.* 53: 122–128.

40. Fixemer, T., K. Remberger, and H. Bonkhoff. 2003. Differential expression of the estrogen receptor beta (ERβ) in human prostate tissue, premalignant changes, and in primary, metastatic, and recurrent prostatic adenocarcinoma. *Prostate.* 54:79–87.

41. Zhang, Y., S. Nojima, H. Nakayama, Y. Jin, and H. Enza. 2003. Characteristics of normal stromal components and their correlation with cancer occurrence in human prostate. *Oncol. Rep.* 10:207–211.

42. Kirschenbaum, A., X. Liu, S. Yao, G. Narla, S. L. Friedman, J. A. Martignetti, and A. C. Levine. 2006. Sex steroids have differential effects on growth and gene expression in primary human prostatic epithelial cell cultures derived from the peripheral vs. transition zones. *Carcinogenesis.* 27:216–224.

43. Diem, M., M. Romeo, S. Boydston-White, M. Miljković, and C. Matthäus. 2004. A decade of vibrational micro-spectroscopy of human cells and tissue (1994–2004). *Analyst.* 129:880–885.